



# Influence of free-stream turbulence intensity on static and dynamic stall of a NACA 0018 aerofoil

Luca Damiola<sup>\*</sup>, Muhammad Faheem Siddiqui, Mark Charles Runacres, Tim De Troyer

*Vrije Universiteit Brussel (VUB), Faculty of Engineering, Thermo and Fluid Dynamics (FLOW), Pleinlaan 2, 1050, Brussels, Belgium*

*Brussels Institute for Thermal-Fluid Systems and clean Energy (BRITE), Vrije Universiteit Brussel (VUB) and Université Libre de Bruxelles (ULB), Belgium*

## ARTICLE INFO

### Keywords:

Unsteady aerodynamics  
Pitching aerofoil  
Free-stream turbulence  
Dynamic stall  
Wind tunnel testing

## ABSTRACT

In many engineering applications, aerofoils experience elevated free-stream turbulence levels. The present work experimentally investigates the effect of free-stream turbulence on the aerodynamic characteristics of a sinusoidally pitching NACA 0018 aerofoil at the transitional Reynolds number of  $2.8 \times 10^5$ . Wind tunnel tests are conducted in quasi-static and dynamic conditions at different turbulence intensities between 0.3% and 8.2%, considering reduced frequencies up to 0.1. The dynamic experiments investigate multiple angle-of-attack ranges in order to quantify the influence of free-stream turbulence in the attached-flow regime, in the stalled regime, and in-and-out of stall. The study demonstrates that high free-stream turbulence drastically changes the flow physics over the aerofoil for both static and dynamic conditions, producing large deviations in the lift and moment coefficients. The quasi-static experiment performed at low free-stream turbulence features a large stall hysteresis linked to the breakdown of the leading-edge laminar separation bubble, whereas static hysteresis is not present at higher turbulence levels. Moreover, dynamic experiments at high angles of attack show a strong dependency on the incoming turbulence intensity, which is found to delay flow separation during the upstroke and enhance reattachment during the downstroke. The work also reveals the intrinsic difficulty of predicting the dynamic stall behaviour under different turbulence conditions, and gives insight into why the existing empirical dynamic stall models are unlikely to succeed in accurately predicting the aerodynamic loads across different onset turbulence intensities.

## 1. Introduction

In many engineering applications, aerofoils experience significant free-stream turbulence levels. Typical examples include wind turbine blades which operate under a wide variety of different onset turbulence intensities because of atmospheric conditions and topographical factors, or due to wakes generated by other wind turbines. While offshore wind turbines generally operate in a low turbulence environment (Bodini et al., 2020), land-based turbines typically experience higher turbulence mainly due to surface roughness effects in the atmospheric boundary layer; in particular, urban flows are characterised by turbulence intensities that can easily go beyond 10% (Janajreh et al., 2013).

One of the primary engineering challenges related to the installation and operation of wind turbines concerns the unsteady aerodynamic loads on the blades, which experience time-varying angles of attack because of gusts, wind shear, and yaw misalignment. Free-stream turbulence is an additional factor which can lead to larger aerodynamic loads that might cause premature failing. A better understanding of

the impact of these unsteady loads is therefore crucial to extend the operational lifetime of wind turbines.

The present work experimentally investigates the unsteady aerodynamic loads of a pitching NACA 0018 aerofoil, which is often used on Vertical Axis Wind Turbines (VAWT) given its good aerodynamic and structural properties. The primary objective is to analyse the effect of free-stream turbulence intensity on static and dynamic stall of a thick aerofoil in order to describe the flow physics involved and obtain an accurate prediction of the unsteady loads acting on the wing. The moderate Reynolds number selected for this study,  $Re = 2.8 \times 10^5$ , is representative of the operating conditions typically encountered by small VAWTs. In this regime, the flow is defined as transitional and wind tunnel experiments are particularly challenging because of their high sensitivity to test conditions such as incoming turbulence, model surface roughness and experimental uncertainties (Melani et al., 2019).

Previous experimental investigations have analysed the physics of pitching aerofoils at different Reynolds number and reduced frequency (McCroskey, 1981; Mulleners and Raffel, 2013). However,

<sup>\*</sup> Corresponding author at: Vrije Universiteit Brussel (VUB), Faculty of Engineering, Thermo and Fluid Dynamics (FLOW), Pleinlaan 2, 1050, Brussels, Belgium.  
E-mail address: [luca.damiola@vub.be](mailto:luca.damiola@vub.be) (L. Damiola).

**Table 1**

List of selected experimental studies of aerofoils with elevated onset turbulence.

Author	Aerofoil	Re [ $\times 10^3$ ]	Type <sup>a</sup>	$k$	AoA [°]	$I_u$ [%]
Mueller et al. (1983)	Lissaman 7769	[150, 300]	s	0	[−20, 25]	[0.08, 0.3]
Hoffmann (1990)	NACA 0015	250	s	0	[−5, 35]	[0.25, 9]
Swalwell et al. (2001)	NACA 0021	350	s	0	[0, 90]	[0.6, 7]
Devinant et al. (2002)	NACA 65 <sub>4</sub> -421	[100, 700]	s	0	[−10, 90]	[0.5, 16]
Amandolèse and Széchényi (2004)	NACA 63 <sub>4</sub> -421	1000	s/d	[0, 0.183]	[0, 30]	[1.1, 7.5]
Kamada et al. (2011)	DU93-W-210	350	s/d	[0, 0.087]	[−20, 50]	[0.15, 11]
Yu et al. (2017)	NACA 0015	4.5	s/d	[0, 0.27]	[−30, 30]	[0.5, 6.9]
Kay et al. (2020)	NACA 0012 & 4412	[50, 200]	s	0	[−6, 20]	[1.3, 15]
Li and Hearst (2021)	NREL S826	400	s	0	[−8, 18]	[0.4, 5.4]
Present study	NACA 0018	280	s/d	[0.0006, 0.100]	[−26, 28]	[0.3, 8.2]

<sup>a</sup>s: static d: dynamic.

little information is available on how free-stream turbulence can affect pitching aerofoils' performance; very often the analysis is limited to static experiments (Mueller et al., 1983; Hoffmann, 1990; Swalwell et al., 2001; Devinant et al., 2002; Li and Hearst, 2021), or it is restricted to a few dynamic cases (Kamada et al., 2011; Yu et al., 2017). Table 1 contains a list of relevant experimental studies which investigate the effect of free-stream turbulence ( $I_u$ ) on the aerodynamic characteristics of different aerofoils, and provides details regarding the corresponding test conditions. Mueller et al. (1983) experimentally analysed the static characteristics of a Lissaman 7769 aerofoil at low Reynolds number, and showed the extreme sensitivity of the boundary layer to the free-stream disturbance environment. Similarly, Swalwell et al. (2001) investigated the static stall behaviour of a NACA 0021 aerofoil at moderate Reynolds number, and concluded that the addition of turbulence was responsible for stall delay. Kamada et al. (2011) studied the effect of turbulence on a DU93-W-210 aerofoil for two dynamic cases, but the analysis did not investigate the influence of the reduced frequency. Amandolèse and Széchényi (2004) provided a good insight on the static and dynamic analysis of a NACA 63<sub>4</sub>-421 aerofoil for different flow turbulence levels; the study was conducted at high Reynolds number and demonstrated that turbulence was responsible for delaying trailing edge stall and increasing the maximum lift coefficient. More recently, Kay et al. (2020) compared the performance of a symmetrical NACA 0012 with a cambered NACA 4412 at low Reynolds number (between 50,000 and 200,000) for elevated turbulence intensity, and demonstrated that camber might be detrimental to maintaining performance in highly unsteady flows.

Besides the experimental studies, the literature abounds with numerical simulations of pitching aerofoils (Visbal and Garmann, 2018; Geng et al., 2018). However, a challenging aspect of numerical simulations is the difficulty to generate free-stream turbulence with the desired intensity and integral length scale at the leading edge of the aerofoil (Wu, 2017; Gilling et al., 2009). Moreover, in spite of the high accuracy of the current numerical methods, high-fidelity simulations inherently involve the realisation of an extremely limited number of cycles and thus may lack the statistical insight that experiments can offer, which is particularly relevant for dynamic stall characterisation (Ramasamy et al., 2021).

The primary goal of this work is therefore to expand the limited knowledge available on dynamic pitching experiments in the transitional regime at elevated free-stream turbulence, in order to understand to what extent turbulence can affect the aerodynamic performance of an aerofoil and whether dynamic stall under turbulent inflow can be predicted from a combination of dynamic experiments at low turbulence intensity and static experiments at high turbulence intensity.

The remainder of the paper is structured as follows. Section 2 is devoted to the description of the experimental campaign and includes a thorough analysis of the inflow conditions. Subsequently, in Section 3 the main results are illustrated and discussed in detail, with particular emphasis on the dynamic experiments. Finally, Section 4 draws the conclusions of the work and indicates possible future developments.

## 2. Methodology

### 2.1. Experimental setup

The experimental campaign was conducted in the low-speed wind tunnel facility of the Vrije Universiteit Brussel. The tunnel is a blow-down open-circuit wind tunnel, with a rectangular inlet test section 2 m wide and 1 m high. The test chamber is 12 m long and has a slightly divergent ceiling (opening angle  $\theta = 0.29^\circ$ ) in order to compensate for the boundary layer growth. The maximum wind velocity is 20 m/s, the turbulence level is around 0.3%. The experimental setup, which is illustrated in Fig. 1(a), consists of a wing having a NACA 0018 aerofoil with chord  $c = 300$  mm and span  $b = 530$  mm. The wing is composed of a central 3D printed section, which contains the pressure taps, and two lateral carbon fibre parts. The wing is connected to the lateral wall of the tunnel through a 300 mm long circular rod, and an actuation system imposes a pitching motion around the mid-chord. In addition, two identical circular endplates are installed at the wing tip and at the wing root in order to minimise three-dimensional effects. The diameter of the endplates is 11.5 times larger than the maximum thickness of the wing, in accordance to the requirements given in Kubo et al. (1989). The setup allows a wide variety of angle of attack time series such as harmonic oscillations, swept sines, multisines, and even random noise, most of the signals with a band limited to about 5 Hz. The motion of the wing is controlled via a dSpace® real-time controller running at 2 kHz, and the output data is resampled at 200 Hz to match the sampling frequency of the pressure measurement system. The wing is equipped with 47 pressure taps (see Fig. 1(b)) located at mid-span in a 3D printed section, and a ZOC33/64Px Scanivalve® pressure measurement system is used for data acquisition at a sampling frequency equal to 200 Hz. The length of the tubing, 400 mm, is kept to a minimum in order to minimise the distortions. Given the absence of a pressure tap at the trailing edge, the pressure value at  $x/c = 1$  has been obtained by linear extrapolation of the pressure on the upper and lower surface of the aerofoil.

Different levels of longitudinal free-stream turbulence intensity ranging from 0.3% to 8.2% were obtained by positioning the square-mesh grid shown in Fig. 1(c) at a proper distance upstream of the test section, in accordance to Molina et al. (2019). The grid is built of wooden boards which are 7 cm wide, and the mesh size of the grid is 35 cm; the ratio between the open area and the total area of the test section is 0.63.

In this work, a sinusoidal motion is prescribed to the wing through the following incidence law:

$$\alpha(t) = \alpha_0 + \alpha_1 \sin(2\pi f t) \quad (1)$$

where  $\alpha_0$  is the mean angle of attack,  $\alpha_1$  is the pitch amplitude and  $f$  is the oscillating frequency. The solid blockage ratio normalised by the full test section ranges between 4.5% and 7% for every imposed motion. In this analysis it was decided not to apply wind tunnel corrections to account for blockage effects since no well-established methods are available for aerofoils undergoing unsteady pitching motions.

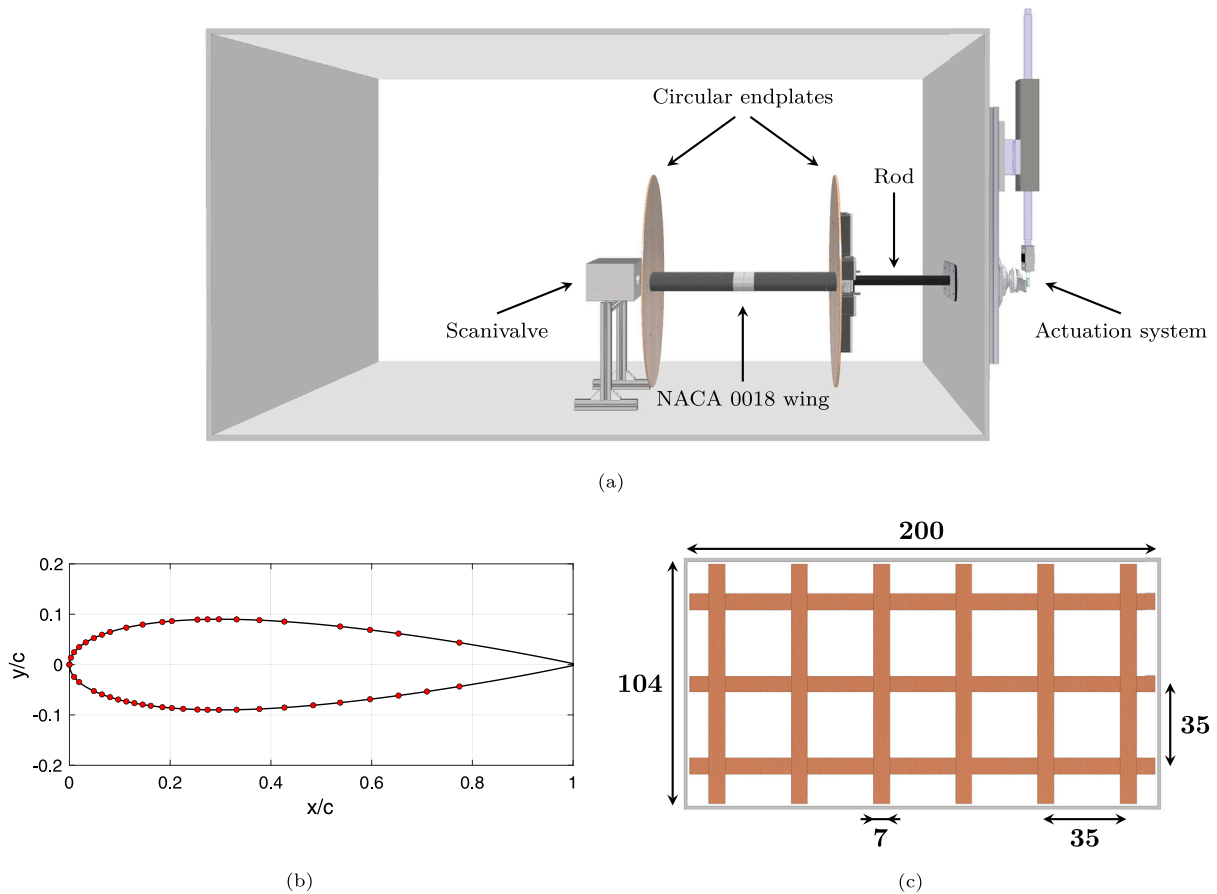


Fig. 1. (a) Frontal view of the experimental setup, (b) location of the pressure taps on the aerofoil, (c) wooden grid for turbulence generation (dimensions given are in cm).

Results have been obtained by phase-averaging data over the available pitching cycles. Lift and moment coefficients of the aerofoil were calculated by numerical integration of the pressure distribution at midspan, taking into account both the normal-to-chord and parallel-to-chord force components.

## 2.2. Free-stream flow characterisation

Tests were conducted at a free-stream velocity  $U_\infty = 15$  m/s, corresponding to a chord-based Reynolds number  $Re = 2.8 \times 10^5$ . The free-stream velocity was evaluated through a pitot tube connected to a Setra model 239 pressure transducer and placed 1 m upstream of the leading edge of the wing. The grid for turbulence generation, when present, was located at least 2.75 m upstream of the pitot tube, depending on the desired turbulence intensity. Turbulence measurements were acquired using a dual-sensor hot-wire probe (Dantec Dynamics 55P61) connected to two identical MiniCTA systems. A traverse system carrying the X-wire probe was employed to characterise the flow in the wind tunnel without the model in a section orthogonal to the main flow direction and located at a streamwise coordinate corresponding to the leading edge of the wing. Data were acquired over a total of 104 (13 × 8) measurement points across the section, at a sampling frequency  $F_s = 25.6$  kHz. The sampling time was set to 10 s for the measurements performed without turbulence grid, and to 15 s for the high turbulence level. The measured area covers a width of 1.68 m and a height of 0.63 m, leading to a spatial resolution of 14 cm and 9 cm, respectively. All three velocity components were measured with the X-wire probe by conducting two separate experiments and rotating the probe around its axis by 90°. In the present work, turbulence intensity

is defined in the longitudinal direction ( $I_u$ ), lateral direction ( $I_v$ ), and vertical direction ( $I_w$ ) according to the following notation:

$$I_u = \frac{u'}{U_\infty} \quad I_v = \frac{v'}{U_\infty} \quad I_w = \frac{w'}{U_\infty} \quad (2)$$

where  $u'$ ,  $v'$  and  $w'$  represent the standard deviation of the velocity fluctuations in the  $x$ ,  $y$  and  $z$  coordinate, respectively. The flow field is presented in Fig. 2 as contour plots in terms of normalised mean velocity and turbulence intensity evaluated in the streamwise direction. Note that the measurement points are represented on the plots as black dots and a linear interpolation is performed among them. The location of the wing relative to the tunnel is reported as a black rectangle. As for the low turbulence case, Fig. 2(a), the flow field presents a good level of uniformity across the section, with a value of turbulence intensity  $I_u \approx 0.3\%$  in most of the investigated region. Although measurements were not taken in close proximity of the wind tunnel walls, the points closest to the lateral and bottom walls highlight the presence of a thick boundary layer, which is responsible for the local increase in turbulence intensity in those regions. As far as the high turbulence case is concerned, Fig. 2(b), the addition of the upstream grid slightly affects flow uniformity, with the left part of the test section that exhibits values of longitudinal velocity generally smaller than the right side. However, the velocity magnitude in the area of interest in proximity of the wing location shows only minor variations of about two percent. The interaction between the turbulence grid and the boundary layer of the lateral walls produces a thickening of the boundary layer, which leads to an enlarged low-velocity and highly-turbulent region near the lateral walls of the tunnel. It is worth noting that the experimental setup comprises two circular endplates, whose main purpose is to minimise the three-dimensional wing tip effects, but also to avoid any possible ingestion of the boundary layer flow. Table 2 summarises and

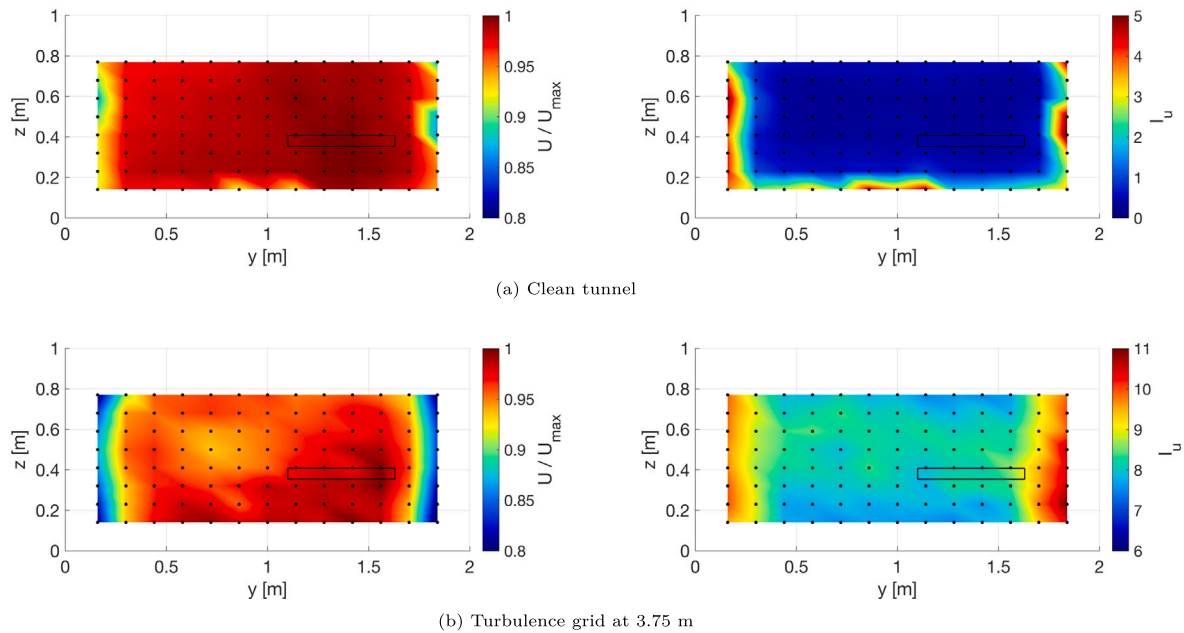


Fig. 2. Normalised longitudinal mean velocity and turbulence intensity measured in the test section without the wing model.

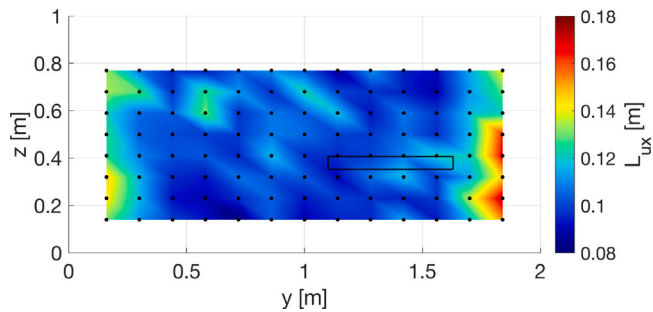


Fig. 3. Contour of the longitudinal integral length scale.

Table 2

Turbulence intensity at the wing position.

	$I_u$ [%]	$I_v$ [%]	$I_w$ [%]
Clean tunnel	0.32	0.30	0.26
Turbulence grid	8.19	7.83	7.65

quantitatively compares the turbulence intensity at the wing position in the longitudinal, lateral and vertical direction, considering the wind tunnel in the clean configuration as well as with the addition of the turbulence grid at a distance of 3.75 m. Note that the presented values represent the average over the four measurement points closest to the wing location.

To further characterise the turbulence generated by the grid, the longitudinal integral length scale ( $L_{ux}$ ) is calculated through the auto-correlation function and assuming Taylor's frozen turbulence hypothesis (Taylor, 1938). The corresponding contour plot computed across the test section is illustrated in Fig. 3. The average over the four points closest to the wing location reveals an integral length scale  $L_{ux} = 0.11$  m, value which is also confirmed by fitting the measured spectrum to the von Kármán spectrum, similar to what is done in Molina et al. (2019). Moreover, this result is in positive agreement with the one obtained from the empirical expression given by Roach (1987), according to which the integral length scale depends on the distance of the grid and on the dimension of its bars.

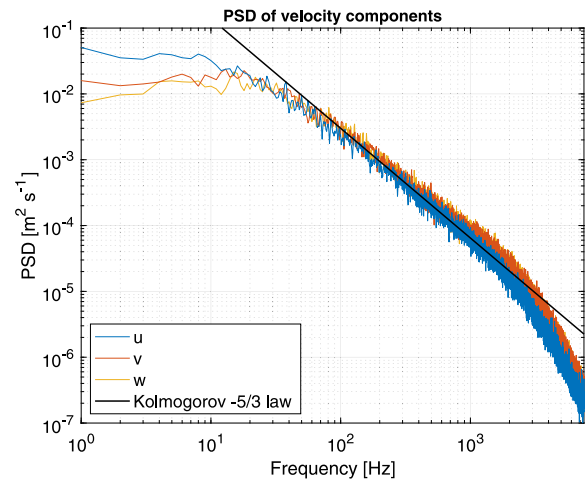


Fig. 4. Turbulence spectra computed at the wing position at a distance of 3.75 m from the grid.

Finally, the power spectral density (PSD) of the velocity fluctuations  $u$ ,  $v$  and  $w$  is computed using the MATLAB<sup>®</sup> algorithm *pwelch*. Fig. 4 illustrates the turbulence spectra calculated at the wing position at a distance of 3.75 m from the grid, showing positive agreement with the  $-5/3$  Kolmogorov law for the inertial subrange.

### 3. Results and discussion

#### 3.1. Quasi-static experiments

Before the analysis of the unsteady cases, quasi-static measurements were acquired for three different levels of free-stream turbulence intensity: 0.3% (clean tunnel), 5.6% and 8.2%. The two high-turbulence cases were obtained by positioning the wooden grid 5 m and 3.75 m upstream of the leading edge of the wing, respectively. Quasi-static experiments were performed by imposing a pitching motion at a sufficiently low reduced frequency  $k = (\pi f c)/U_\infty = 0.0006$ , corresponding to an equivalent reduced pitch rate  $r_{eq} = \alpha_1(\pi/180)k = 2.8 \times 10^{-4}$ . It has



been known for many decades that the rate of change of aerofoil incidence strongly affects the maximum lift coefficient and the stall angle (Martin et al., 1974; Carr et al., 1977; McCroskey, 1982; Ramasamy et al., 2016). We followed the recommendations from Le Fouest et al. (2021) to assure that the chosen pitch rate for the quasi-static experiments is suitable to correctly capture the static loads and the static stall angle. For the present quasi-static analysis, the mean angle of attack was set to  $\alpha_0 = 0^\circ$ , with a pitch amplitude of  $\alpha_1 = 26^\circ$ . Lift and moment coefficients have been obtained by phase-averaging data over three subsequent periods, using bins of  $1^\circ$  amplitude for the entire angle-of-attack range except for the low turbulence intensity experiment, where bins of  $0.5^\circ$  were employed in the stall region (upstroke,  $[20.5^\circ\text{--}22.5^\circ]$ ) and in the reattachment region (downstroke,  $[12.5^\circ\text{--}14.0^\circ]$ ) to accurately capture the abrupt variations in the aerodynamic coefficients. This choice assures a good balance between resolution and number of samples in each bin. Fig. 5 illustrates the lift and pitching moment coefficient as a function of the angle of attack for all considered turbulence levels. Note that the error bars representing the standard deviation of the aerodynamic coefficients are indicated in the plots every two bins, in order to improve the readability of the figure. Results from the literature obtained at a similar Reynolds number are also reported for comparison. Given the symmetry of the selected aerofoil, the following description focuses on the positive angles of attack only.

As far as the lift coefficient is concerned, Fig. 5(a), the most striking difference among the considered free-stream turbulence intensities is the presence of a large static hysteresis which is visible for  $I_u = 0.3\%$  only (black curve). In this case, an abrupt leading-edge stall takes place at  $\alpha = 21^\circ$  causing a sudden loss of lift, with the  $C_l$  dropping to 0.48. In the post-stall phase, the boundary layer remains separated for a significant portion of the pitch-down motion until the angle of attack reduces to  $\alpha = 13.5^\circ$ . The static hysteresis implies the presence of two stable flow configurations, with the flow selecting one or the other branch based on its initial state. This flow feature can be ascribed to the development and subsequent bursting of a laminar separation bubble (LSB) on the suction side of the aerofoil in the leading-edge region. The relation between the static hysteresis and the breakdown of the LSB which causes full leading-edge stall is also reported in Williams et al. (2017) for the same aerofoil shape and similar flow conditions. The presence of the LSB can be identified in the pressure distribution as a plateau: Fig. 6 shows that the LSB is present only in the case of low free-stream turbulence intensity and it moves towards the leading edge for increasing angles of attack. No sign of the bubble could be detected post stall. The bubble was also absent in the first part of the pitch-down phase until flow reattachment around  $\alpha = 13.5^\circ$ , when it reappeared. For higher turbulence levels (5.6% and 8.2%), the absence of the LSB prevents the formation of the static hysteresis, and a light stall behaviour with a more gradual reduction of the lift coefficient can be observed. In addition, stall is delayed and the maximum  $C_l$  is increased by approximately 5% ( $I_u = 5.6\%$ ) and 10% ( $I_u = 8.2\%$ ) with respect to the low turbulence case.

At low angles of attack,  $[0^\circ\text{--}7^\circ]$ , a change in free-stream turbulence intensity does not significantly modify the slope of the  $C_l - \alpha$  curve. On the other hand, the close-up view reported in Fig. 7(a) highlights that in the angle-of-attack range  $[7^\circ\text{--}10^\circ]$  a local lift-slope increase is evident at low turbulence intensity, whereas it is not present at higher free-stream turbulence levels. According to Timmer (2008), the kink in the lift curve is caused by the presence of a laminar separation bubble on the pressure side near the trailing edge, which increases the effective camber of the wing and causes a stronger lift growth; the study also demonstrates that the addition of zigzag tape on the lower surface at 70% of the chord forces transition and eliminates the bump. In the present work, the coarse resolution of pressure taps in the trailing-edge region prevents the direct detection of the lower surface laminar separation bubble. However, the authors believe that the laminar separation bubble is present and affects the flow conditions around the entire

aerofoil, as indicated in literature. This assumption is further confirmed by the expected continuous behaviour of the lift curves associated with the higher turbulence intensities,  $I_u = 5.6\%$  and  $I_u = 8.2\%$ . In these two experiments, the larger free-stream disturbances are responsible for an upstream shift in laminar-turbulent transition (Istvan and Yarusevych, 2018), which prevents the formation of a laminar separation bubble on the pressure side as well as on the suction side of the aerofoil. The pitching moment coefficient, Fig. 7(b), further corroborates this insight. Indeed, when the lower surface LSB appears in the trailing-edge region around  $\alpha = 7^\circ$ , the increased apparent camber causes the moment coefficient to drop. When the incidence is increased to approximately  $\alpha = 11^\circ$ , the flow over the entire lower surface of the aerofoil becomes laminar, and the virtual increase in camber due to the separation bubble disappears, producing a growth of the moment coefficient. As is the case with the lift curves, this particular behaviour in the  $[7^\circ\text{--}13^\circ]$  range is completely absent in the moment curves at higher turbulence intensities (orange and blue curves), since there is no bubble. At larger angles of attack, all three curves exhibit a slope reduction which is believed to be caused by the onset of trailing edge stall. This feature is more pronounced in the case of low free-stream turbulence since the laminar boundary layer is more prone to flow separation.

The present results obtained for different turbulence levels show the same qualitative behaviour demonstrated by Hoffmann (1990) for a NACA 0015; both studies demonstrate that for increasing turbulence intensity stall is delayed, the maximum lift coefficient is augmented, and the static hysteresis disappears. For low turbulence intensity, results are also compared with data available in the literature. Two experimental investigations conducted by Timmer (2008) and Strangfeld et al. (2015) on a NACA 0018 aerofoil confirm the presence of a large stall hysteresis. However, this flow feature is found to be very sensitive to test conditions: for the same Reynolds number and almost identical turbulence intensity, the experiments of Timmer predict stall at  $\alpha = 17^\circ$ , whereas Strangfeld et al. observe it around  $\alpha = 20^\circ$ . This demonstrates the challenging nature of flows in the transitional regime, which are strongly affected by test conditions such as surface roughness, turbulence intensity, proximity of wind tunnel walls, etc.

The major difference between the literature and the present study lies in the slope of the lift curve, and in the more pronounced bump in the  $C_l - \alpha$  curve that can be detected around  $\alpha = 7^\circ$  in Timmer (2008) and Strangfeld et al. (2015). It is believed that in the present study the absence of such a strong kink in the  $C_l - \alpha$  curve is mainly caused by the different free-stream turbulence conditions and, possibly, by minor imperfections of the wing model. The experiments used for comparison have been performed at a significantly lower free-stream turbulence level (0.05%–0.1%), even compared to the low turbulence case of the present study (0.3%). This discrepancy can be crucial for transitional flows, which are known to be very sensitive to test conditions; it is believed that the higher turbulence level of the present work hinders the formation of a lower surface laminar separation bubble, with an important effect on the lift slope. Although the different turbulence intensity is regarded as the major source of discrepancy with the literature, the overall difference in the lift slope may be partly attributed to the proximity of the model with the wind tunnel walls, with top and bottom walls of the tunnel being located at a distance from the wing equal to  $2.1c$  and  $1.2c$ , respectively. Moreover, it should be noted that in both prior studies the wing model is mounted directly on the lateral walls of the wind tunnel and spans the entire width of the test section, whereas in the present investigation finite circular endplates are used to suppress wing-tip vortices.

Similar to the lift coefficient, the quarter-chord moment coefficient illustrated in Fig. 5(b) shows a strong dependency on the free-stream turbulence intensity: for  $I_u = 0.3\%$  a clockwise static hysteresis is identified in the angle-of-attack range  $13.5^\circ < \alpha < 21.0^\circ$ , whereas a qualitatively different behaviour is visible at the higher turbulence

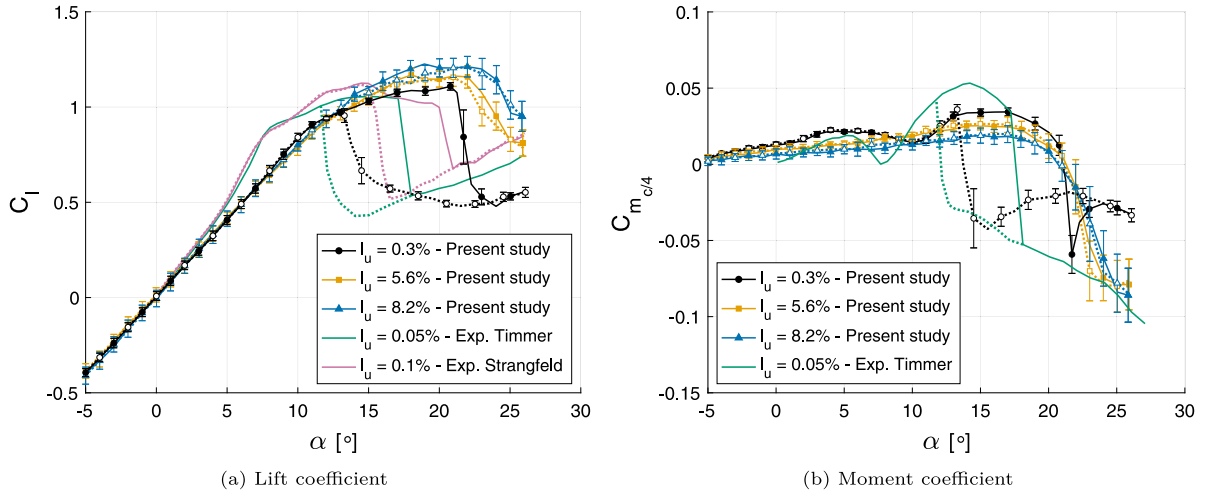


**Fig. 5.** Lift coefficient and quarter-chord moment coefficient of a NACA 0018 aerofoil at  $Re = 2.8 \times 10^5$  for different free-stream turbulence intensities. Solid lines indicate pitch-up motion, dotted lines indicate pitch-down, and error bars represent standard deviation. Note that Timmer (2008) and Strangfeld et al. (2015) provide data for  $Re = 3 \times 10^5$  and positive angles of attack only.

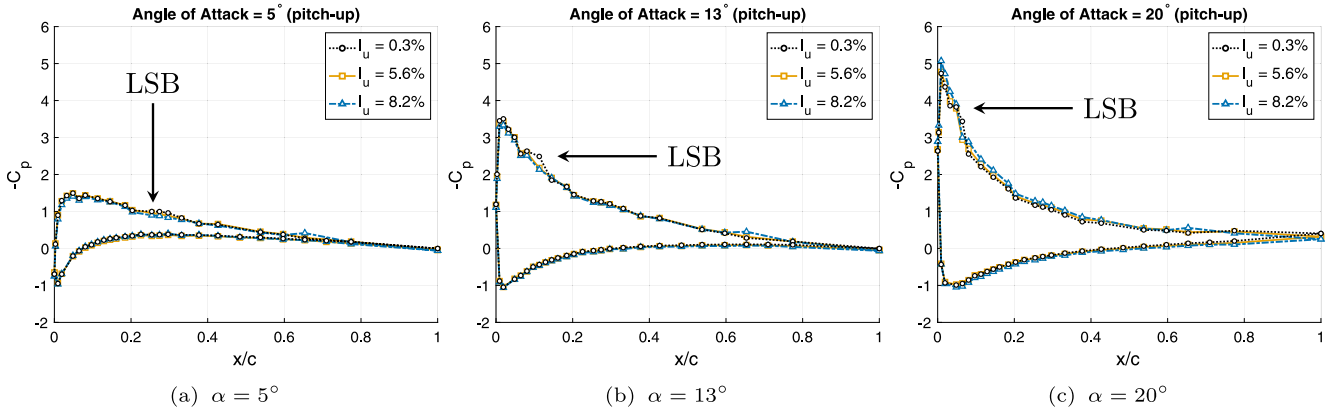


**Fig. 6.** Pressure coefficient distribution for different angles of attack with focus on the laminar separation bubble present for  $I_u = 0.3\%$ . Pressure values are evaluated considering angle-of-attack bins of  $0.4^\circ$ .

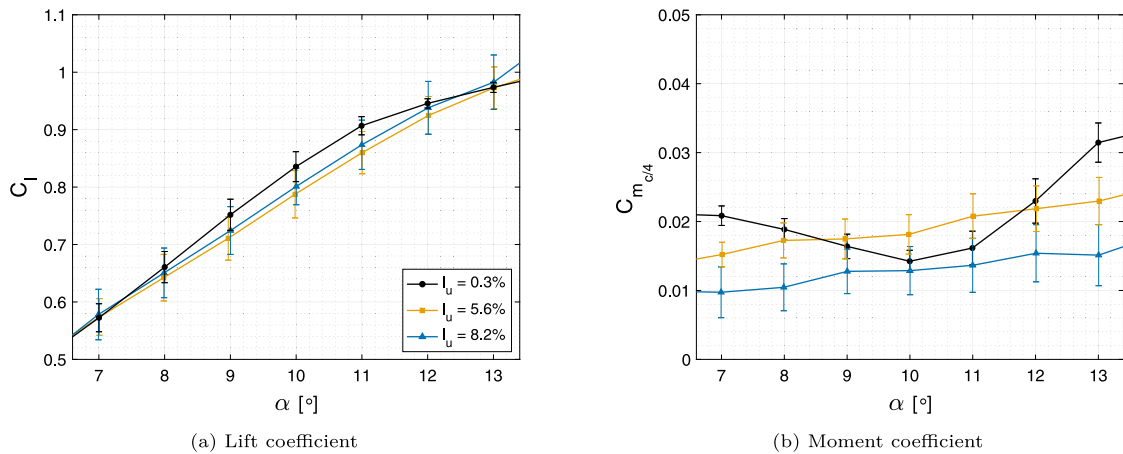


**Fig. 7.** Close-up views of lift coefficient and quarter-chord moment coefficient during pitch-up motion for the three considered free-stream turbulence intensities. (For interpretation of the references to colour in this figure legend, the reader is referred to the web version of this article.)

levels ( $I_u = 5.6\%$  and  $I_u = 8.2\%$ ), where the hysteresis is completely eliminated.

For the low turbulence case, the comparison with Timmer's results confirms the presence of a clockwise moment hysteresis occurring at the same angle-of-attack range of the lift hysteresis. For moderate

angles of attack, the  $C_m - \alpha$  curve exhibits a positive slope suggesting that the aerodynamic centre is located slightly upstream of the quarter-chord point. Around  $\alpha = 10^\circ$  a reduction in the moment coefficient can be detected as a consequence of the presence of a minor lower surface laminar separation bubble close to the trailing edge. This flow feature

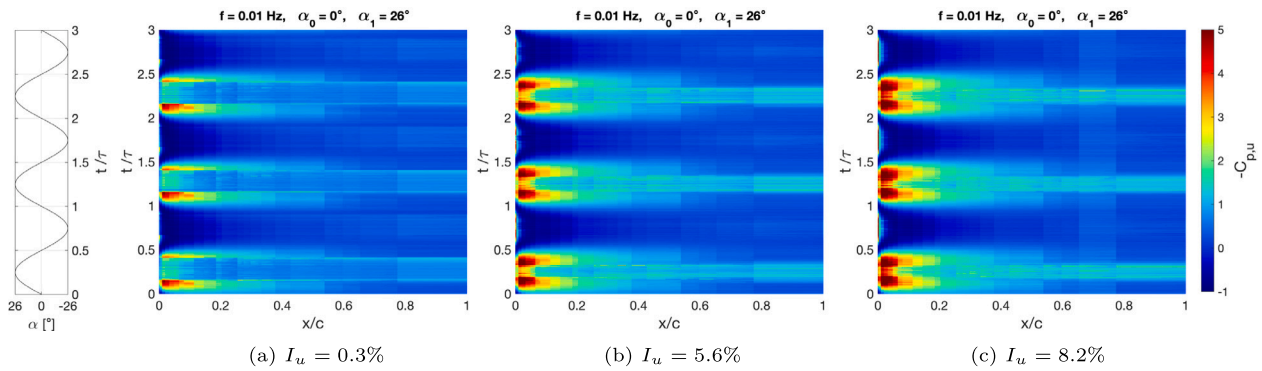


Fig. 8. Upper surface pressure coefficient as a function of dimensionless time ( $t/\tau$ ) and chord ( $x/c$ ).

is much more evident in Timmer's experiments around  $\alpha = 8^\circ$ , given the more pronounced lower surface laminar separation bubble clearly visible also from the lift curve. At high angles of attack, following the abrupt stall, the moment coefficient becomes negative and shows a decreasing behaviour for increasing incidence. Unfortunately, no information concerning the moment coefficient in the experiments of Strangfeld et al. is available in the literature.

Fig. 8 shows the contours of the upper surface pressure coefficient as a function of the dimensionless coordinate  $x/c$  ( $x$ -axis) and of the dimensionless time  $t/\tau$  ( $y$ -axis), where  $\tau$  represents the period of oscillation. For every free-stream turbulence intensity, three complete cycles are performed, and minor differences are detected between them. While the two high turbulence experiments (Fig. 8(b) and (c)) show a very similar flow pattern, the low turbulence case (Fig. 8(a)) is qualitatively different. Indeed, for  $I_u = 0.3\%$  the contour plot exhibits a sharp drop in the upper surface pressure coefficient during pitch-up at approximately  $\alpha = 21^\circ$ , indicating the occurrence of an abrupt leading-edge stall. Moreover, flow reattachment can be clearly identified during pitch-down around  $\alpha = 13.5^\circ$ . These flow features are qualitatively different in the high turbulence cases, in which stall is delayed, reattachment occurs at a higher angle of attack during the downstroke, and the pressure coefficient in the leading edge region varies more gradually. Fig. 9 highlights the pressure distribution around the aerofoil at high angles of attack, and quantifies the difference in the pressure coefficient between the lowest and the highest considered turbulence intensity. For both cases, mean values and corresponding standard deviations were obtained considering angle-of-attack bins of  $0.4^\circ$ . At  $\alpha = 23^\circ$ , Fig. 9(a), for  $I_u = 0.3\%$  the flow on the upper surface is fully separated, with a modest negative pressure peak  $C_p = -1.59$  at the leading edge and a constant pressure coefficient from  $x/c = 0.065$  until the trailing edge. On the contrary, for  $I_u = 8.2\%$  the flow is still attached and the pressure coefficient presents a strong suction peak  $C_p = -5.10$  in proximity of the leading edge. At  $\alpha = 25^\circ$ , Fig. 9(b), massive flow separation occurs even at high turbulence intensity, but the pressure coefficient on the suction side remains larger compared to the low turbulence case, resulting in higher lift. It should be noted that the experiments performed at high turbulence intensity show larger pressure fluctuations compared to the low turbulence experiments, where pressure taps generally register values characterised by a smaller standard deviation.

### 3.2. Dynamic experiments

A key parameter describing the degree of flow separation over a given pitching aerofoil is represented by the maximum angle of attack (McCroskey, 1981) and, more specifically, by its relation with the static stall angle,  $\alpha_{ss}$ . Additionally, other variables play an important role in determining the unsteady flow behaviour over a pitching aerofoil: the most relevant are aerofoil geometry, frequency and amplitude of oscillation, free-stream turbulence intensity and Reynolds number.

Table 3

List of dynamic experiments.

Experiment #	$\alpha_0$ [°]	$\alpha_1$ [°]	$\alpha_{\max} - \alpha_{ss}$ [°]	$f$ [Hz]	$k$ [-]	$I_u$ [%]	P [-]
1a	12	6	-3	0.4	0.025	0.3	32
1b	12	6	-5	0.4	0.025	8.2	32
2a	12	6	-3	1	0.063	0.3	40
2b	12	6	-5	1	0.063	8.2	40
3a	12	6	-3	1.6	0.100	0.3	48
3b	12	6	-5	1.6	0.100	8.2	48
4a	18	6	+3	0.4	0.025	0.3	32
4b	18	6	+1	0.4	0.025	8.2	32
5a	18	6	+3	1	0.063	0.3	40
5b	18	6	+1	1	0.063	8.2	40
6a	18	6	+3	1.6	0.100	0.3	48
6b	18	6	+1	1.6	0.100	8.2	48
7a	22	6	+7	0.4	0.025	0.3	32
7b	22	6	+5	0.4	0.025	8.2	32
8a	22	6	+7	1	0.063	0.3	40
8b	22	6	+5	1	0.063	8.2	40
9a	22	6	+7	1.6	0.100	0.3	48
9b	22	6	+5	1.6	0.100	8.2	48

The present section provides a comprehensive analysis of multiple dynamic experiments where the maximum angle of attack is varied between  $18^\circ$  (pre-stall) and  $28^\circ$  (post-stall), thus considering the attached-flow regime, the stalled regime, and in-and-out of stall. Furthermore, particular attention is given to the effect of two other parameters, namely free-stream turbulence intensity and frequency of oscillation.

In light of the similarity of the static results obtained for  $I_u = 5.6\%$  and  $I_u = 8.2\%$ , it was decided to perform dynamic experiments in the clean tunnel ( $I_u = 0.3\%$ ) and at the highest turbulence level ( $I_u = 8.2\%$ ) only. As for the frequency of oscillation, experiments are conducted at three different values of reduced frequency between 0.025 and 0.1. Table 3 summarises all the considered dynamic cases and provides details regarding angle-of-attack range, frequency of oscillation, turbulence intensity and number of periods (P).

#### 3.2.1. Case 1: $\alpha(t) = 12^\circ + 6^\circ \sin(2\pi ft)$

The present section analyses the case in which the maximum angle of attack reached during the dynamic cycle,  $\alpha_{\max} = 18^\circ$ , is lower than the static stall angle. The characteristic feature of these experiments is that the flow remains attached during the entire cycle, for both low and high free-stream turbulence. The main results are presented in Fig. 10, which illustrates the influence of free-stream turbulence intensity and reduced frequency on the lift and quarter-chord moment coefficient. Note that the graphs show the mean values and the corresponding standard deviation bands evaluated over the available cycles (using all periods as indicated in Table 3, except for the first one which was removed to avoid transients), and, in case of the lift coefficient, the static lift curves are also reported for comparison.

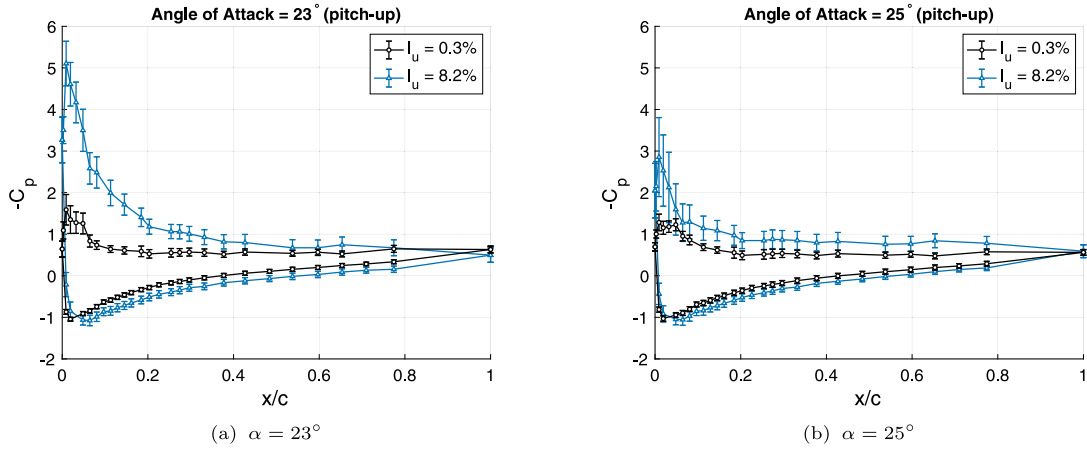


Fig. 9. Pressure coefficient distribution at high angles of attack: error bars represent standard deviation.

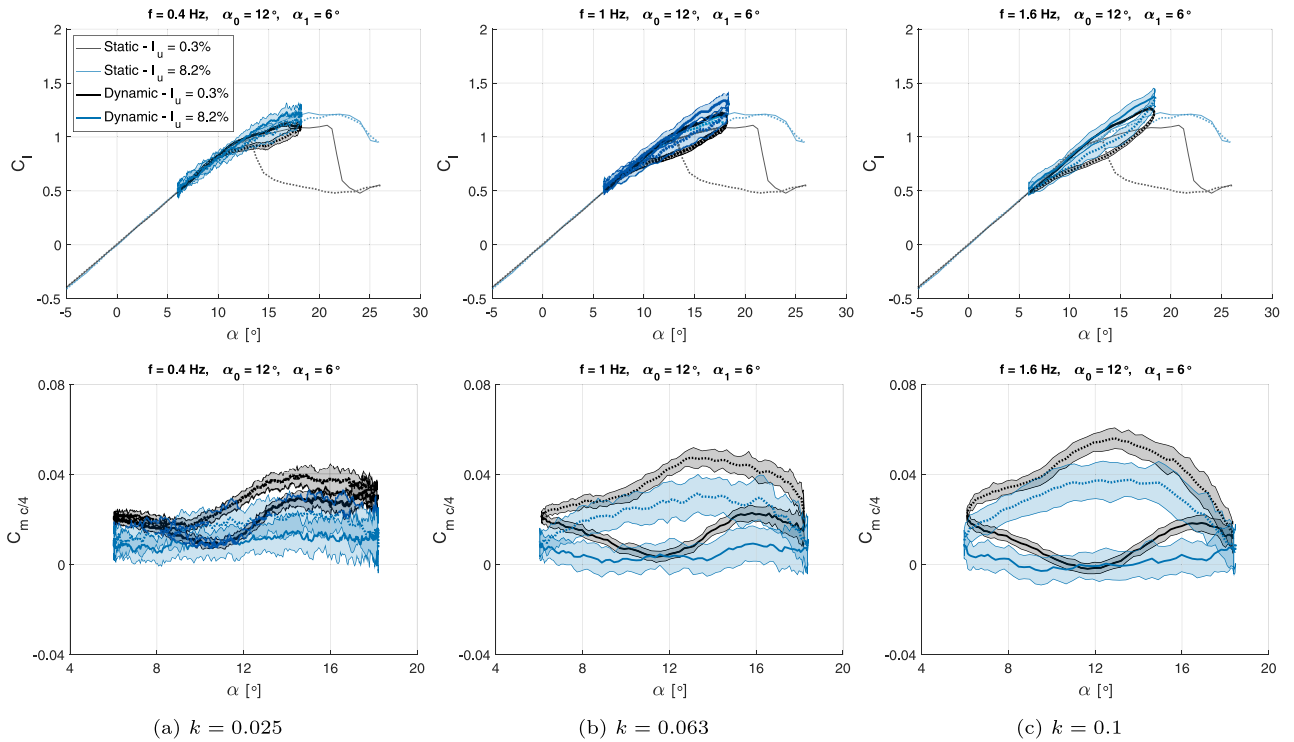


Fig. 10. Lift coefficient and quarter-chord moment coefficient for different values of reduced frequency and turbulence intensity ( $\alpha_0 = 12^\circ$ ); solid lines indicate pitch-up motion, dotted lines indicate pitch-down.

For low reduced frequency  $k = 0.025$ , Fig. 10(a), the dynamic lift curve is very close to the quasi-static curve for both turbulence levels. On the contrary, for increasing values of reduced frequency, Fig. 10(b) and (c), the lift coefficient starts to deviate from its static counterpart, showing a larger clockwise dynamic hysteresis loop. Moreover, during the upstroke the slope of the  $C_l - \alpha$  curves becomes steeper with increasing reduced frequency, exhibiting values for the lift coefficient larger than the static ones. These effects, which are particularly evident at the highest reduced frequency  $k = 0.1$ , are a direct consequence of the unsteady motion of the aerofoil. During the upstroke, the dynamic motion is responsible for a reduction in adverse pressure gradient over most of the aerofoil, which delays flow separation and produces higher lift. Additionally, the pitch-up motion causes a relevant momentum input to the boundary layer near the leading edge, which contributes in delaying separation (Dimitriadis, 2017). The opposite effect is obtained during the downstroke, since the pitch-down motion enhances

separation at the leading edge, resulting in late reattachment and a consequent enlargement in the lift hysteresis loop.

As far as the moment coefficient is concerned, the  $C_m - \alpha$  curves exhibit a counter-clockwise hysteresis loop, which significantly increases in size at high values of reduced frequency. The area enclosed in the cycle variation of the pitching moment coefficient has been traditionally used to analyse the stability of the air load system, since it is proportional to the aerodynamic damping (Corke and Thomas, 2015). More specifically, Carta and Niebanck (1969) and Oates (1989) defined the dimensionless cycle aerodynamic damping,  $\Xi_{\text{cycle}}$ , as

$$\Xi_{\text{cycle}} = -\frac{C_W}{\pi \alpha_1^2} = -\frac{1}{\pi \alpha_1^2} \oint C_{m c/4} d\alpha \quad (3)$$

where  $C_W$  is the coefficient of work done by the quarter-chord aerodynamic moment over one pitching cycle and  $\alpha_1$  is the amplitude of oscillation. According to Eq. (3), positive aerodynamic damping is obtained for counter-clockwise moment hysteresis loops, whereas



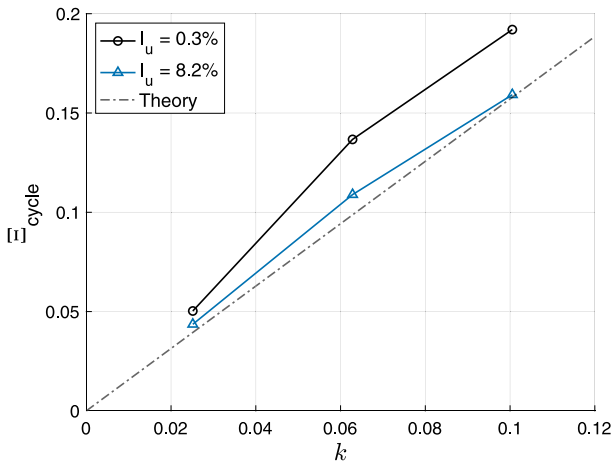


Fig. 11. Dimensionless aerodynamic damping as a function of the reduced frequency.

clockwise loops produce negative aerodynamic damping. All the experiments shown in Fig. 10 exhibit a positive aerodynamic damping, which grows in magnitude for increasing frequency. As illustrated in Fig. 11, these results are consistent with Theodorsen's unsteady thin-airfoil (flat plate) theory (Theodorsen, 1935), which is valid for aerofoils undergoing pure harmonic pitch oscillations about the quarter-chord in a potential flow, when the maximum angle of attack reached during the dynamic motion is below the static stall angle; the theory always predicts a positive aerodynamic damping, which is linearly dependent on the reduced pitching frequency, namely  $\Xi_{\text{cycle}} = \pi k/2$ .

### 3.2.2. Case 2: $\alpha(t) = 18^\circ + 6^\circ \sin(2\pi f t)$

Fig. 12 illustrates the case where the maximum angle of attack is larger than the static stall angle, and it shows a strong dependency on the incoming turbulence intensity. The experiment conducted at low free-stream turbulence level represents a typical example of the deep dynamic stall regime, which is characterised by the formation of a Dynamic Stall Vortex (DSV) in the leading-edge region. The DSV is shed from the leading edge and it is then convected downstream over the suction side of the aerofoil, producing instantaneous values of lift and moment significantly higher than the static ones. The DSV leaving the trailing edge produces an abrupt drop in lift and moment coefficient. During the vortex-shedding process, the thickness of the viscous layer is of the order of the aerofoil chord (McCroskey, 1982). Deep dynamic stall is encountered by VAWTs that operate at low tip-speed ratio; although in this regime VAWTs can achieve the largest power production, deep dynamic stall is generally not desired in normal operating conditions since it causes severe forces and vibrations that can harm structural integrity (Le Fouest and Mulleners, 2022; Carr and Chandrasekhara, 1996).

In our experiments, at low turbulence intensity an abrupt stall occurs and a large hysteresis in the aerodynamic loads is noticeable. In the post-stall phase, the flow remains separated during the entire pitch-down motion and recovers during pitch-up only. On the contrary, in case of high free-stream turbulence, stall is more gentle and turbulence is found to encourage flow reattachment during the downstroke. While the lift coefficient during upstroke is comparable between low and high free-stream turbulence intensities, a remarkable difference is evident during the pitch-down motion, with the  $C_l$  dropping to values below 0.5 in case of low turbulence intensity. This is clearly visible in Fig. 13, which depicts the mean pressure coefficient distribution and its standard deviation at  $\alpha = 18^\circ$ , for a reduced frequency  $k = 0.063$ . For low turbulence intensity, Fig. 13(a), the flow is attached during pitch-up ( $C_l = 1.23$ ), whereas full separation occurs during pitch-down ( $C_l = 0.44$ ). Conversely, Fig. 13(b) shows that for high turbulence intensity

the flow at the considered angle of attack has reattached, producing a less severe lift reduction from  $C_l = 1.34$  to  $C_l = 0.96$ . It should also be noted that a higher turbulence intensity leads to increased pressure fluctuations, resulting in a larger standard deviation.

As for the maximum lift coefficient, it reaches increasingly higher values for growing reduced frequency. For  $k = 0.025$ , compared to the static case, the maximum  $C_l$  is 7.9% higher for the low turbulence case and 10.6% higher for high free-stream turbulence, whereas for  $k = 0.1$  the  $C_l$  reaches much larger values (26.8% and 27.5% higher, respectively) showing the potential beneficial effects of dynamic stall in VAWTs.

Additional insight into the dynamic stall characteristics is provided by the  $C_m - \alpha$  curves shown in Fig. 12. For low turbulence intensity, the quarter-chord moment coefficient exhibits a large clockwise hysteresis loop, leading to strong negative aerodynamic damping. On the other hand, for elevated turbulence intensity the moment coefficient shows a moderate clockwise hysteresis loop at high angles of attack and a counter-clockwise loop as soon as the incidence reduces below  $20^\circ$ , resulting in a positive net aerodynamic damping.

The experiment illustrated in Fig. 12(b) is further investigated by means of pressure contours. More specifically, Fig. 14 depicts the instantaneous values of the upper surface pressure coefficients for two consecutive representative periods, for both levels of turbulence intensities. Besides an expected qualitatively different pressure distribution, a crucial difference between the two cases concerns the presence of the dynamic stall vortex, which only appears at low turbulence intensity, Fig. 14(a). In this case, the convection of the DSV over the aerofoil can be identified as a suction peak which moves over time along the aerofoil chord. The shedding of the DSV is followed by an abrupt reduction in the suction generated in the leading edge region of the aerofoil, which causes a sudden drop in lift and a large negative (nose-down) pitching moment. It is important to remark that a clear trace of the vortex can be detected in 85% of the cycles. However, given the inherently highly unsteady nature of this phenomenon, cycle-to-cycle variations are identified in the location of formation of the primary DSV, which is formed in the range of angles of attack  $[23.0^\circ - 23.8^\circ]$ . Moreover, as can be inferred from Fig. 14(a), the intrinsically stochastic behaviour of the vortex shedding process leads to a significant variability in the post-stall load fluctuations. It should be noted that even at high turbulence intensity the trace of the DSV can be detected in 20% of the cycles. Based on the slope of the dashed lines in Fig. 14(a), it is possible to estimate the propagation velocity of the DSV vortex along the aerofoil chord. The calculated value is equal to  $0.40 U_\infty$ , corresponding to 2.5 convective timescales of the flow. Similarly, the propagation velocity of the DSV is computed for the two other oscillating frequencies. At the lowest reduced frequency,  $k = 0.025$  ( $r_{eq} = 0.0026$ ), the propagation velocity is equal to  $0.28 U_\infty$ , whereas at the highest reduced frequency,  $k = 0.1$  ( $r_{eq} = 0.0105$ ), it is equal to  $0.50 U_\infty$ . Results are in general agreement with previous studies Lorber and Carta (1987), Chandrasekhara and Carr (1990) and Wei et al. (2021), which demonstrated that the propagation velocity of the DSV increases with pitch rate. Finally, it is important to consider that the coarse resolution of pressure taps near the trailing-edge makes it hard to identify the DSV in that region, thus increasing the uncertainty of the vortex velocity, which can be estimated to be approximately equal to  $\pm 0.05 U_\infty$ .

It appears evident that the dynamic results at high turbulence intensity cannot be readily retrieved from a straightforward combination of dynamic cases at low turbulence and static experiments at high turbulence, since the addition of turbulence completely alters the flow field, especially at high angles of attack. Existing empirical dynamic stall models are therefore unlikely to succeed in accurately predicting the aerodynamic loads across different onset turbulence intensities.

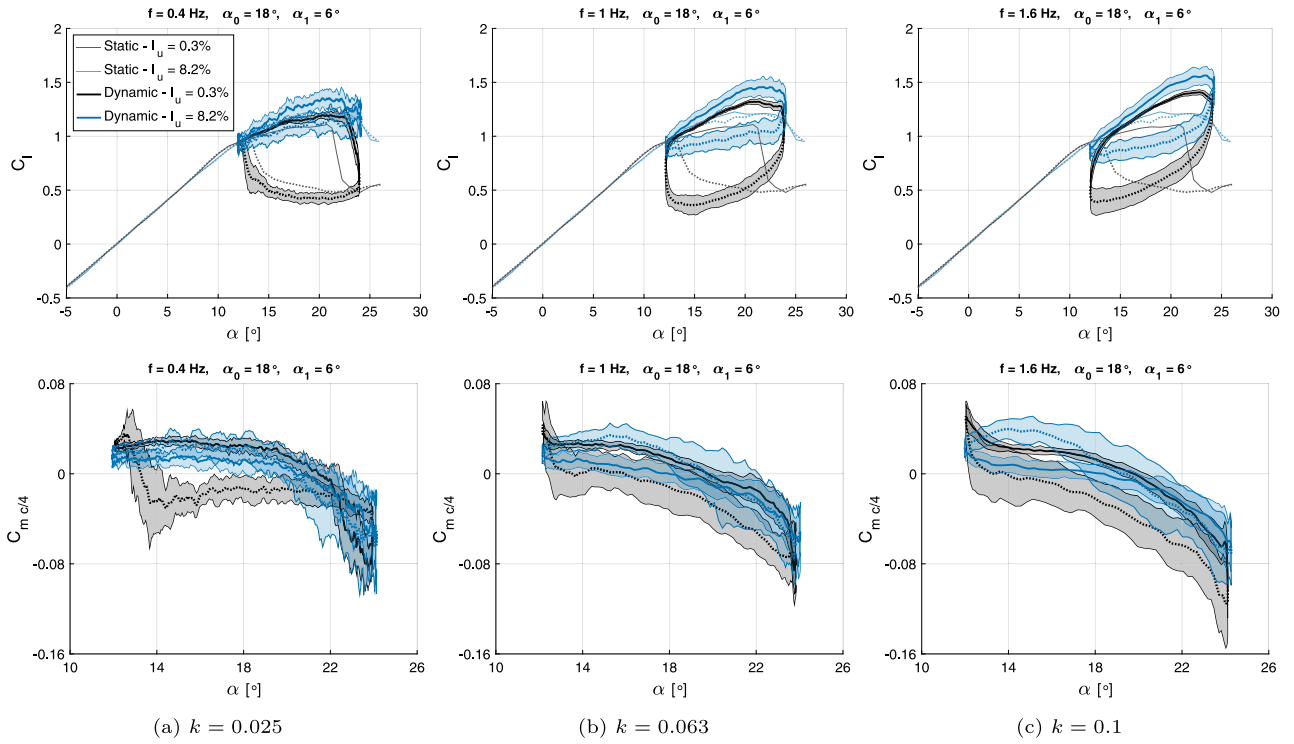


Fig. 12. Lift coefficient and quarter-chord moment coefficient for different values of reduced frequency and turbulence intensity ( $\alpha_0 = 18^\circ$ ); solid lines indicate pitch-up motion, dotted lines indicate pitch-down.

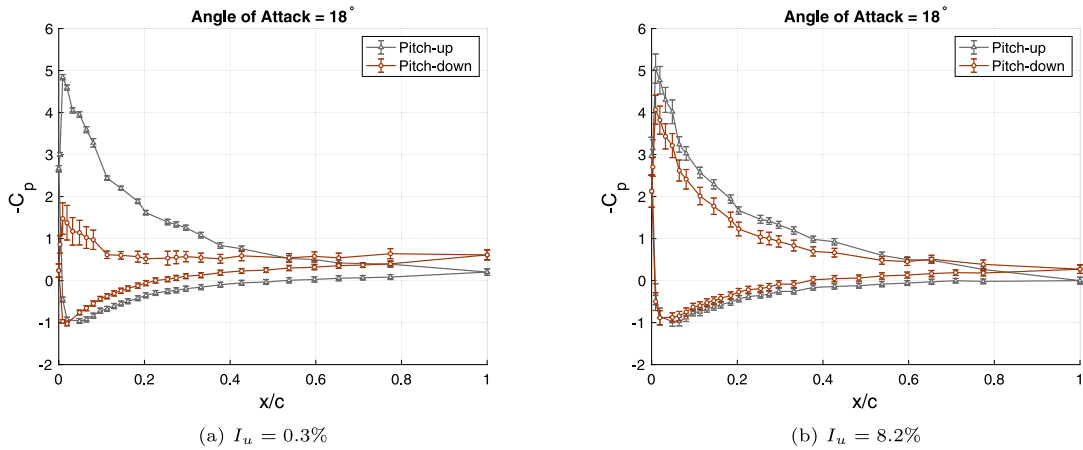


Fig. 13. Pressure coefficient distribution at  $\alpha = 18^\circ$  ( $k = 0.063$ ). Mean values and corresponding standard deviations are evaluated considering an angle-of-attack bin of  $0.4^\circ$ .

### 3.2.3. Case 3 : $\alpha(t) = 22^\circ + 6^\circ \sin(2\pi ft)$

In this case the maximum angle of attack is far beyond the static stall angle. This experiment is of particular interest since the lowest angle of attack reached during the dynamic cycle ( $\alpha_{\min} = 16^\circ$ ) is above the angle of attack where reattachment takes place in static conditions at low free-stream turbulence ( $\alpha = 13.5^\circ$ ).

Fig. 15 illustrates the main results in terms of lift coefficient and quarter-chord moment coefficient. The role of free-stream turbulence is crucial, since it completely changes the degree of flow separation on the aerofoil. Indeed, in the experiment conducted at low free-stream turbulence the flow is fully separated during the entire cycle; there is no reattachment since the considered angle-of-attack range is always above the reattachment angle of attack in static conditions. On the other hand, at high turbulence intensity the flow is attached for most of the pitch-up phase, and the curve is qualitatively similar to the dynamic experiments discussed in Section 3.2.2, but with a much larger hysteresis loop. In this case, at the highest reduced frequency  $k = 0.1$

the maximum lift coefficient is 25% higher than its static counterpart. Moreover, it can be noted that for both turbulence levels an increase in reduced frequency leads to a considerable enlargement of the lift hysteresis loop.

The analysis of the quarter-chord moment coefficient provides additional information on the underlying flow field. For  $I_u = 0.3\%$ , the  $C_m - \alpha$  curves exhibit a counter-clockwise hysteresis loop, which increases in size with the reduced frequency and leads to a large positive aerodynamic damping. On the other hand, for  $I_u = 8.2\%$  the hysteresis loop features a more complex behaviour, characterised by a net aerodynamic damping which is close to zero.

To further understand the origin of the differences in the aerodynamic coefficients across the turbulence intensities, a deeper analysis is conducted on the pressure distribution around the aerofoil at high angle of attack. Fig. 16 illustrates the mean pressure coefficient distribution and its standard deviation at  $\alpha = 22^\circ$ , for a reduced frequency  $k = 0.063$ . For low turbulence intensity, Fig. 16(a), the flow is fully separated

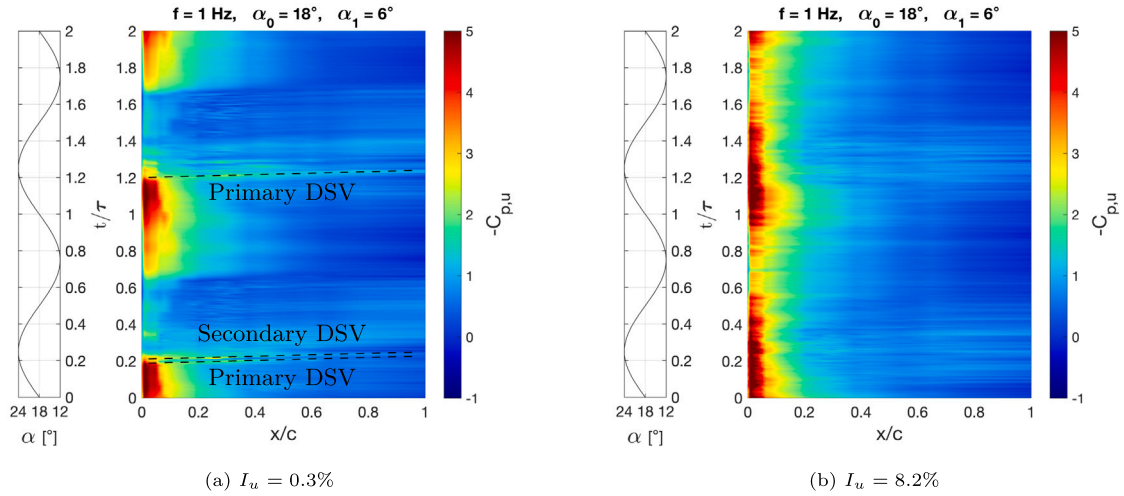


Fig. 14. Upper surface pressure coefficient as a function of dimensionless time ( $t/\tau$ ) and chord ( $x/c$ ) for two consecutive representative periods. The presence of the dynamic stall vortex is indicated by a dashed line.

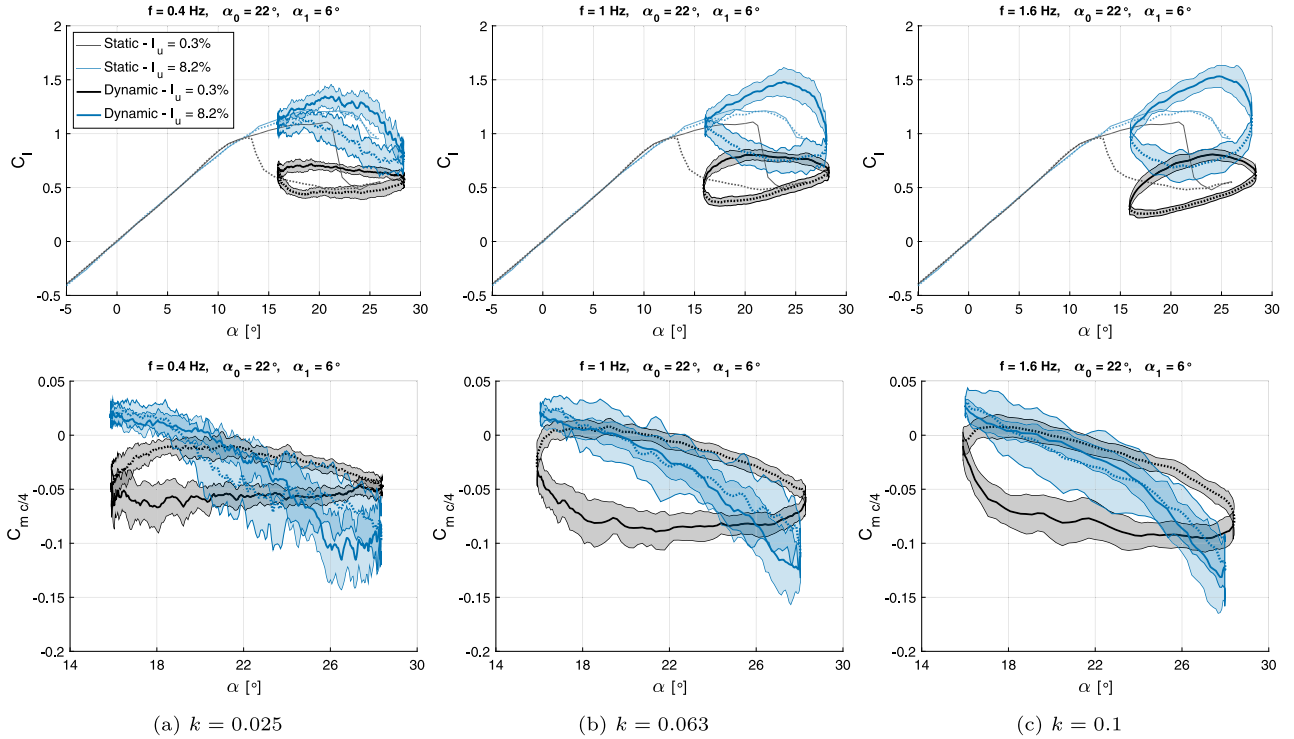


Fig. 15. Lift coefficient and quarter-chord moment coefficient for different values of reduced frequency and turbulence intensity ( $\alpha_0 = 22^\circ$ ); solid lines indicate pitch-up motion, dotted lines indicate pitch-down.

during both pitch-up and pitch-down. The difference between the two curves is only related to the dynamic motion of the aerofoil, which, at the considered incidence, is characterised by the maximum pitch rate. Conversely, Fig. 16(b) shows that for high turbulence intensity the flow is attached during upstroke, whereas flow separation only occurs during downstroke. When comparing the pitch-down curves across the two different turbulence intensities, it can be noted that the highly turbulent and energetic flow still generates stronger suction in the leading-edge region even though the flow is clearly separated. Moreover, while in this case the region of zero pressure gradient only extends after  $x/c = 0.20$ , at low turbulence intensity the flattening of the curve starts already at  $x/c = 0.065$ , indicating massive flow separation over the majority of the aerofoil.

### 3.2.4. Effect of free-stream turbulence intensity on laminar–turbulent transition

Free-stream turbulence plays a key role in determining the aerodynamic performance of an aerofoil, significantly modifying the aerodynamic coefficients and the degree of flow separation. According to Mayle (1991), free-stream turbulence intensity and pressure gradient are the most important parameters that determine the onset of transition on a given aerofoil, whereas surface roughness, surface curvature, compressibility, and heat transfer generally produce secondary effects. In the present experiments, the availability of unsteady pressure measurements is used to estimate laminar–turbulent transition. More specifically, the standard deviation of the pressure coefficient is computed to identify the approximate location of the transition point on the upper surface (suction side) of the aerofoil. Similarly to Raiola et al.

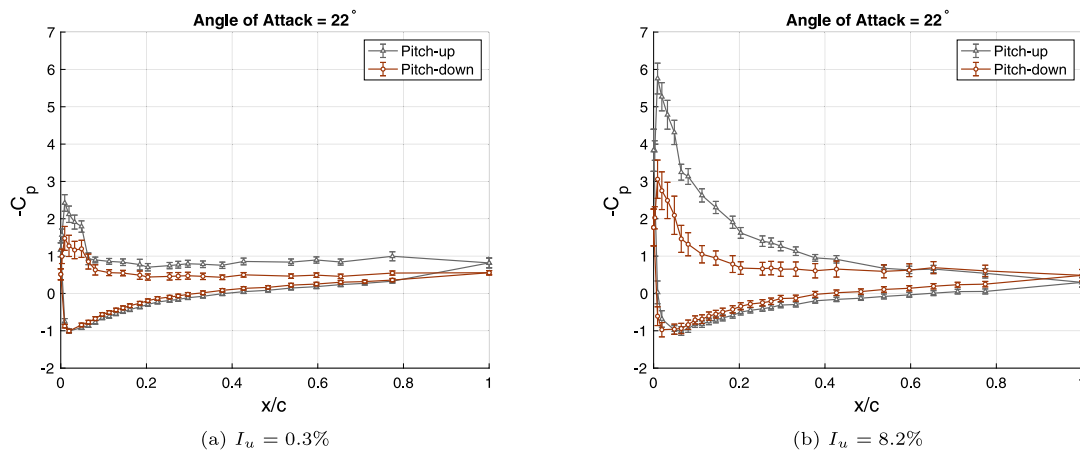


Fig. 16. Pressure coefficient distribution at  $\alpha = 22^\circ$  ( $k = 0.063$ ). Mean values and corresponding standard deviations are evaluated considering an angle-of-attack bin of  $0.4^\circ$ .

(2018), the movement of the transition point is detected from the peaks in the standard deviation. For this investigation, it has been chosen to analyse the experiment previously shown in Fig. 10(a), where the flow remains attached during the entire dynamic loop and results are phase-averaged over 32 cycles. The considered case is described by the angle-of-attack law  $\alpha(t) = 12^\circ + 6^\circ \sin(2\pi f t)$ , where  $f = 0.4$  Hz. Fig. 17 depicts the contours of the standard deviation of the upper surface pressure coefficient as a function of the dimensionless coordinate  $x/c$  and of the dimensionless time  $t/\tau$ , and demonstrates a crucial difference between the two considered turbulence levels.

For low turbulence intensity, Fig. 17(a), a sinusoidal pattern can be identified, and the peak of the pressure fluctuations defining the transition point moves with the same frequency of the pitching aerofoil. At  $t/\tau = 0$  ( $\alpha = 12^\circ$ ) the peak of the pressure fluctuations is around  $x/c = 0.2$  and, for increasing incidence, the stronger adverse pressure gradient forces it to move upstream towards the leading edge; at the maximum angle of attack  $\alpha_{\max} = 18^\circ$  corresponding to  $t/\tau = 0.25$ , transition is found to occur around  $x/c = 0.08$ . The subsequent downstroke motion causes the transition point to move downstream, until the minimum angle of attack  $\alpha_{\min} = 6^\circ$  is reached at  $t/\tau = 0.75$ : at this incidence, transition occurs around  $x/c = 0.30$ .

On the other hand, for high turbulence intensity, Fig. 17(b), the standard deviation of the pressure coefficient exhibits its maxima at a fixed coordinate  $x/c = 0.02$ . Therefore, the transition point always remains at the same chordwise location regardless of the pitching motion of the aerofoil, and the boundary layer is turbulent for the vast majority of the chord. In this case, the underlying transition mode is called “bypass” transition, and it is triggered by the large disturbances in the external flow caused by the elevated free-stream turbulence; the typical Tollmien–Schlichting mode of instability is therefore by-passed. This transition mechanism often occurs in gas turbine engines, which involve highly turbulent and unsteady flows (Mayle, 1991), but it is also relevant for wind turbines in urban and complex terrains.

#### 4. Conclusions

The present study has experimentally investigated the effect of free-stream turbulence on the aerodynamic characteristics of a pitching NACA 0018 aerofoil at a Reynolds number of  $2.8 \times 10^5$ . Wind tunnel tests were conducted in quasi-static and dynamic conditions under different longitudinal turbulence intensities between 0.3% and 8.2%. High free-stream turbulence was achieved using a specifically designed grid, and a dual-sensor hot-wire probe was employed to characterise the flow in the tunnel without the model. Quasi-static experiments demonstrated that free-stream turbulence can drastically change the aerofoil stall behaviour. While for low turbulence intensity an abrupt stall occurs and a large static hysteresis is present, high free-stream turbulence

leads to a more gentle stall behaviour characterised by the absence of hysteresis in the aerodynamic loads. A delay in flow separation was also observed at elevated turbulence levels, resulting in a higher maximum lift coefficient.

Furthermore, this work analysed several dynamic experiments in which the combined effect of free-stream turbulence, reduced frequency and angle-of-attack range was taken into account. In the attached flow case, limited differences in lift and moment coefficients were registered among the considered turbulence intensities. Conversely, when the maximum angle of attack was increased beyond the static stall angle, a considerable departure in the aerodynamic coefficients was clearly identified, and turbulence was found to delay separation during upstroke and enhance flow reattachment during downstroke. At high turbulence level, bypass transition was also recognised in proximity of the leading edge of the aerofoil. The study also highlighted that an increase in reduced frequency leads to an increment in maximum lift coefficient and to an enlargement of the lift hysteresis loop. These effects are a direct consequence of the unsteady motion of the aerofoil, which delays flow separation during pitch-up and, additionally, causes late reattachment during pitch-down, with a consequent enlargement of the hysteresis loop.

Moreover, the analysis revealed that dynamic stall at high onset turbulence cannot be readily retrieved from a trivial combination of dynamic stall at low turbulence intensity and static experiments at high turbulence intensity; although this might be valid for specific combinations of experimental parameters, the different flow physics involved makes it impossible to generalise the reasoning to arbitrary dynamic motions and flow conditions. Therefore, existing empirical dynamic stall models are unlikely to succeed in accurately predicting the aerodynamic loads across different onset turbulence intensities.

Finally, the present study demonstrated the potential beneficial effect of free-stream turbulence on the static and dynamic stall behaviour of a NACA 0018 aerofoil at moderate Reynolds number. This consideration is particularly relevant for VAWTs which operate in the atmospheric boundary layer and they are often exposed to highly turbulent flows. However, it is important to underline the high complexity of the flow typically encountered by VAWTs, which is often characterised by time-varying free-stream velocity, cross-flow and finite wing effects. The results herein should therefore only be applied over a limited portion of the blades. Future work should be conducted to further expand and generalise these results to different aerofoil geometries and flow conditions, e.g. with a free-stream velocity that varies sinusoidally in time. The sensitivity of the aerodynamic coefficients to the turbulence integral length scale could also be investigated to further extend these findings.



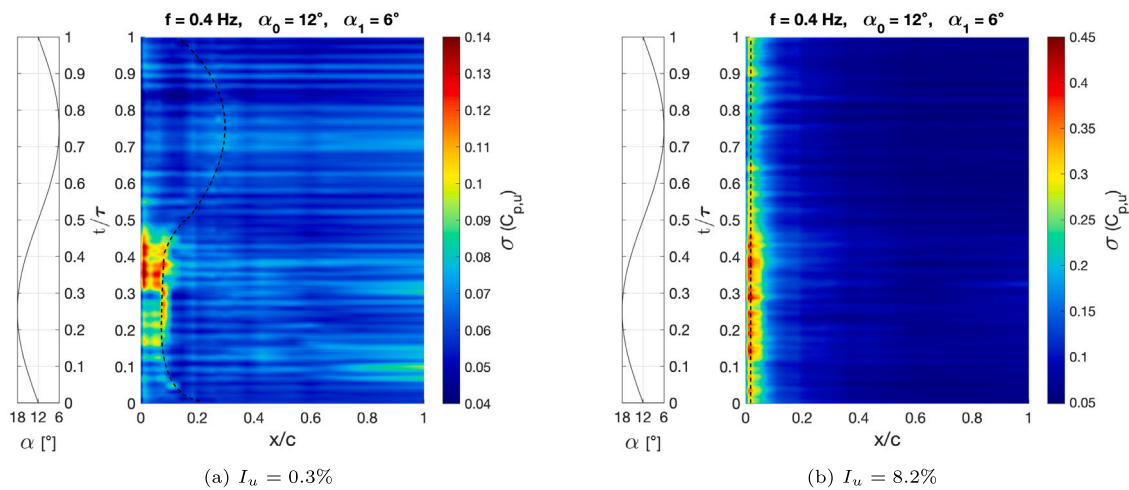


Fig. 17. Standard deviation of the upper surface pressure coefficient as a function of dimensionless time ( $t/\tau$ ) and chord ( $x/c$ ). The approximate location of the laminar–turbulent transition is indicated by the dashed line.

### CRedit authorship contribution statement

**Luca Damiola:** Writing – original draft, Methodology, Investigation, Formal analysis, Visualization. **Muhammad Faheem Siddiqui:** Software, Investigation, Methodology. **Mark Charles Runacres:** Writing – review & editing, Conceptualization, Supervision, Funding acquisition. **Tim De Troyer:** Writing – review & editing, Conceptualization, Methodology, Project administration, Funding acquisition.

### Declaration of competing interest

The authors declare that they have no known competing financial interests or personal relationships that could have appeared to influence the work reported in this paper.

### Data availability

Data will be made available on request.

### Acknowledgements

This research was supported by the FWO, Belgium fellowship with project number 1S90123N. The financial support from the Research Council of the Vrije Universiteit Brussel, Belgium under grant number OZR3821 and SRP60 is gratefully acknowledged.

### References

- Amondolèse, X., Széchenyi, E., 2004. Experimental study of the effect of turbulence on a section model blade oscillating in stall. *Wind Energy* 7 (4), 267–282.
- Bodini, N., Lundquist, J.K., Kirincich, A., 2020. Offshore wind turbines will encounter very low atmospheric turbulence. In: *Journal of Physics: Conference Series*, Vol. 1452. IOP Publishing, 012023.
- Carr, L.W., Chandrasekhara, M., 1996. Compressibility effects on dynamic stall. *Prog. Aerosp. Sci.* 32 (6), 523–573.
- Carr, L.W., McAlister, K.W., McCroskey, W.J., 1977. Analysis of the Development of Dynamic Stall Based on Oscillating Airfoil Experiments. Tech. rep.
- Carta, F.O., Niebanck, C.F., 1969. Prediction of Rotor Instability at High Forward Speeds. Volume 3. Stall Flutter. Tech. rep., United Technologies Corp Stratford CT Sikorsky Aircraft Div.
- Chandrasekhara, M., Carr, L., 1990. Flow visualization studies of the mach number effects on dynamic stall of an oscillating airfoil. *J. Aircr.* 27 (6), 516–522.
- Corke, T.C., Thomas, F.O., 2015. Dynamic stall in pitching airfoils: aerodynamic damping and compressibility effects. *Annu. Rev. Fluid Mech.* 47, 479–505.
- Devinant, P., Laverne, T., Hureau, J., 2002. Experimental study of wind-turbine airfoil aerodynamics in high turbulence. *J. Wind Eng. Ind. Aerodyn.* 90 (6), 689–707.
- Dimitriadis, G., 2017. Introduction to Nonlinear Aeroelasticity. John Wiley & Sons.

- Geng, F., Kalkman, I., Suiker, A., Blocken, B., 2018. Sensitivity analysis of airfoil aerodynamics during pitching motion at a Reynolds number of  $1.35 \times 10^5$ . *J. Wind Eng. Ind. Aerodyn.* 183, 315–332.
- Gilling, L., Sørensen, N., Davidson, L., 2009. Detached eddy simulations of an airfoil in turbulent inflow. In: *47th AIAA Aerospace Sciences Meeting Including the New Horizons Forum and Aerospace Exposition*. p. 270.
- Hoffmann, J., 1990. Effects of onset free-stream turbulence on the performance characteristics of an airfoil. In: *Flight Simulation Technologies Conference and Exhibit*. p. 3025.
- Istvan, M.S., Yarusevych, S., 2018. Effects of free-stream turbulence intensity on transition in a laminar separation bubble formed over an airfoil. *Exp. Fluids* 59 (3), 1–21.
- Janajreh, I., Su, L., Alan, F., 2013. Wind energy assessment: Masdar city case study. *Renew. Energy* 52, 8–15.
- Kamada, Y., Maeda, T., Murata, J., Toki, T., Tobuchi, A., 2011. Effects of turbulence intensity on dynamic characteristics of wind turbine airfoil. *J. Fluid Sci. Technol.* 6 (3), 333–341.
- Kay, N.J., Richards, P.J., Sharma, R.N., 2020. Influence of turbulence on cambered and symmetrical airfoils at low Reynolds numbers. *AIAA J.* 58 (5), 1913–1925.
- Kubo, Y., Miyazaki, M., Kato, K., 1989. Effects of end plates and blockage of structural members on drag forces. *J. Wind Eng. Ind. Aerodyn.* 32 (3), 329–342.
- Le Fouest, S., Deparday, J., Mulleners, K., 2021. The dynamics and timescales of static stall. *J. Fluids Struct.* 104, 103304.
- Le Fouest, S., Mulleners, K., 2022. The dynamic stall dilemma for vertical-axis wind turbines. *Renew. Energy*.
- Li, L., Hearst, R.J., 2021. The influence of freestream turbulence on the temporal pressure distribution and lift of an airfoil. *J. Wind Eng. Ind. Aerodyn.* 209, 104456.
- Lorber, P.F., Carta, F.O., 1987. Unsteady Stall Penetration Experiments at High Reynolds Number. Tech. rep., United Technologies Research Center East Hartford CT.
- Martin, J., Empey, R., McCroskey, W., Caradonna, F., 1974. An experimental analysis of dynamic stall on an oscillating airfoil. *J. Am. Helicopter Soc.* 19 (1), 26–32.
- Mayle, R.E., 1991. The 1991 IGTI scholar lecture: The role of laminar-turbulent transition in gas turbine engines. *J. Turbomach.* 113 (4), 509–536. <http://dx.doi.org/10.1115/1.2929110>.
- McCroskey, W.J., 1981. The Phenomenon of Dynamic Stall. Tech. rep., National Aeronautics and Space Administration Moffett Field Ca Ames Research Center.
- McCroskey, W.J., 1982. Unsteady airfoils. *Annu. Rev. Fluid Mech.* 14 (1), 285–311.
- Melani, P.F., Balduzzi, F., Ferrara, G., Bianchini, A., 2019. An annotated database of low Reynolds aerodynamic coefficients for the NACA 0018 airfoil. In: *AIP Conference Proceedings*, Vol. 2191. AIP Publishing LLC, 020110.
- Molina, A.C., De Troyer, T., Massai, T., Vergaerde, A., Runacres, M.C., Bartoli, G., 2019. Effect of turbulence on the performance of VAWTs: An experimental study in two different wind tunnels. *J. Wind Eng. Ind. Aerodyn.* 193, 103969.
- Mueller, T.J., Pohlen, L.J., Conigliaro, P.E., Jansen, B.J., 1983. The influence of free-stream disturbances on low Reynolds number airfoil experiments. *Exp. Fluids* 1 (1), 3–14.
- Mulleners, K., Raffel, M., 2013. Dynamic stall development. *Exp. Fluids* 54 (2), 1–9.
- Oates, G.C., 1989. Aircraft Propulsion Systems Technology and Design. AIAA.
- Raiola, M., Discetti, S., Ianiro, A., Samara, F., Avallone, F., Ragni, D., 2018. Smart rotors: Dynamic-stall load control by means of an actuated flap. *AIAA J.* 56 (4), 1388–1401.

- Ramasamy, M., Sanayei, A., Wilson, J.S., Martin, P.B., Harms, T., Nikoueeeyan, P., Naughton, J., 2021. Reducing uncertainty in dynamic stall measurements through data-driven clustering of cycle-to-cycle variations. *J. Am. Helicopter Soc.* 66 (1), 1–17.
- Ramasamy, M., Wilson, J.S., McCroskey, W.J., Martin, P.B., 2016. Measured characteristics of cycle-to-cycle variations in dynamic stall. In: AHS Technical Meeting on Aeromechanics Design for Vertical Lift, San Francisco, CA, Vol. 2022.
- Roach, P., 1987. The generation of nearly isotropic turbulence by means of grids. *Int. J. Heat Fluid Flow* 8 (2), 82–92.
- Strangfeld, C., Rumsey, C.L., Mueller-Vahl, H., Greenblatt, D., Nayeri, C., Paschereit, C.O., 2015. Unsteady thick airfoil aerodynamics: experiments, computation, and theory. In: 45th AIAA Fluid Dynamics Conference. p. 3071.
- Swalwell, K.E., Sheridan, J., Melbourne, W., 2001. The effect of turbulence intensity on stall of the NACA 0021 aerofoil. In: 14th Australasian Fluid Mechanics Conference. pp. 10–14.
- Taylor, G.I., 1938. The spectrum of turbulence. *Proc. R. Soc. Lond. Ser. A Math. Phys. Eng. Sci.* 164 (919), 476–490.
- Theodorsen, T., 1935. General Theory of Aerodynamic Instability and the Mechanism of Flutter. National Advisory Committee for Aeronautics.
- Timmer, W., 2008. Two-dimensional low-Reynolds number wind tunnel results for airfoil NACA 0018. *Wind Eng.* 32 (6), 525–537.
- Visbal, M.R., Garmann, D.J., 2018. Analysis of dynamic stall on a pitching airfoil using high-fidelity large-eddy simulations. *AIAA J.* 56 (1), 46–63.
- Wei, B., Gao, Y., Li, D., 2021. Physics of dynamic stall vortex during pitching oscillation of dynamic airfoil. *Int. J. Aeronaut. Space Sci.* 22 (6), 1263–1277.
- Williams, D.R., Reißner, F., Greenblatt, D., Müller-Vahl, H., Strangfeld, C., 2017. Modeling lift hysteresis on pitching airfoils with a modified Goman-Khrabrov model. *AIAA J.* 55 (2), 403–409.
- Wu, X., 2017. Inflow turbulence generation methods. *Annu. Rev. Fluid Mech.* 49, 23–49.
- Yu, J., Leu, T., Miao, J.-J., 2017. Investigation of reduced frequency and freestream turbulence effects on dynamic stall of a pitching airfoil. *J. Vis.* 20 (1), 31–44.